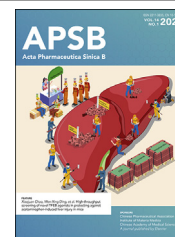




Chinese Pharmaceutical Association
Institute of Materia Medica, Chinese Academy of Medical Sciences

Acta Pharmaceutica Sinica B

www.elsevier.com/locate/apsb
www.sciencedirect.com



ORIGINAL ARTICLE

Mitochondria-specific near-infrared photoactivation of peroxynitrite upconversion luminescent nanogenerator for precision cancer gas therapy



Hui Yu^{a,†}, Aliya Tiemuer^{a,†}, Xufeng Yao^a, Mingyuan Zuo^a,
Hai-Yan Wang^{b,*}, Yi Liu^{a,*}, Xiaoyuan Chen^{c,d,e,f,*}

^aDepartment of Biomedical Engineering, School of Engineering, China Pharmaceutical University, Nanjing 211198, China

^bSchool of Mechanical Engineering, Southeast University, Nanjing 211189, China

^cDepartments of Diagnostic Radiology, Surgery, Chemical and Biomolecular Engineering, and Biomedical Engineering, Yong Loo Lin School of Medicine and College of Design and Engineering, National University of Singapore, Singapore 119074, Singapore

^dClinical Imaging Research Centre, Centre for Translational Medicine, Yong Loo Lin School of Medicine, National University of Singapore, Singapore 117599, Singapore

^eNanomedicine Translational Research Program, Yong Loo Lin School of Medicine, National University of Singapore, Singapore 117597, Singapore

^fInstitute of Molecular and Cell Biology, Agency for Science, Technology, and Research (A*STAR), Proteos, Singapore 138673, Singapore

Received 3 April 2023; received in revised form 27 June 2023; accepted 12 July 2023

KEY WORDS

Near infrared;
Photo-triggered;
Mitochondrion;
Upconversion luminescent
bioimaging;
Peroxynitrite;

Abstract Gas therapy is emerging as a highly promising therapeutic strategy for cancer treatment. However, there are limitations, including the lack of targeted subcellular organelle accuracy and spatio-temporal release precision, associated with gas therapy. In this study, we developed a series of photoactivatable nitric oxide (NO) donors NRh-R-NO (R = Me, Et, Bn, *i*Pr, and Ph) based on an *N*-nitrosated upconversion luminescent rhodamine scaffold. Under the irradiation of 808 nm light, only NRh-Ph-NO could effectively release NO and NRh-Ph with a significant turn-on frequency upconversion luminescence (FUCL) signal at 740 nm, ascribed to lower N–N bond dissociation energy. We also investigated

*Corresponding authors.

E-mail addresses: haiyanwang@seu.edu.cn (Hai-Yan Wang), yiliu@cqu.edu.cn (Yi Liu), chen.shawn@nus.edu.sg (Xiaoyuan Chen).

[†]These authors made equal contributions to this work.

Peer review under the responsibility of Chinese Pharmaceutical Association and Institute of Materia Medica, Chinese Academy of Medical Sciences.

<https://doi.org/10.1016/j.apsb.2023.08.019>

2211-3835 © 2024 The Authors. Published by Elsevier B.V. on behalf of Chinese Pharmaceutical Association and Institute of Materia Medica, Chinese Academy of Medical Sciences. This is an open access article under the CC BY-NC-ND license (<http://creativecommons.org/licenses/by-nc-nd/4.0/>).

Nanogenerator;
Gas therapy;
In vivo

the involved multistage near-infrared-controlled cascade release of gas therapy, including the NO released from NRh-Ph-NO along with one NRh-Ph molecule generation, the superoxide anion $O_2^{\cdot-}$ produced by the photodynamic therapy (PDT) effect of NRh-Ph, and highly toxic peroxyinitrite anion ($ONOO^-$) generated from the co-existence of NO and $O_2^{\cdot-}$. After mild nano-modification, the nanogenerator (NRh-Ph-NO NPs) empowered with superior biocompatibility could target mitochondria. Under an 808 nm laser irradiation, NRh-Ph-NO NPs could induce NO/ROS to generate RNS, causing a decrease in the mitochondrial membrane potential and initiating apoptosis by caspase-3 activation, which further induced tumor immunogenic cell death (ICD). *In vivo* therapeutic results of NRh-Ph-NO NPs showed augmented RNS-potentiated gas therapy, demonstrating excellent biocompatibility and effective tumor inhibition guided by real-time FUCL imaging. Collectively, this versatile strategy defines the targeted RNS-mediated cancer therapy.

© 2024 The Authors. Published by Elsevier B.V. on behalf of Chinese Pharmaceutical Association and Institute of Materia Medica, Chinese Academy of Medical Sciences. This is an open access article under the CC BY-NC-ND license (<http://creativecommons.org/licenses/by-nc-nd/4.0/>).

1. Introduction

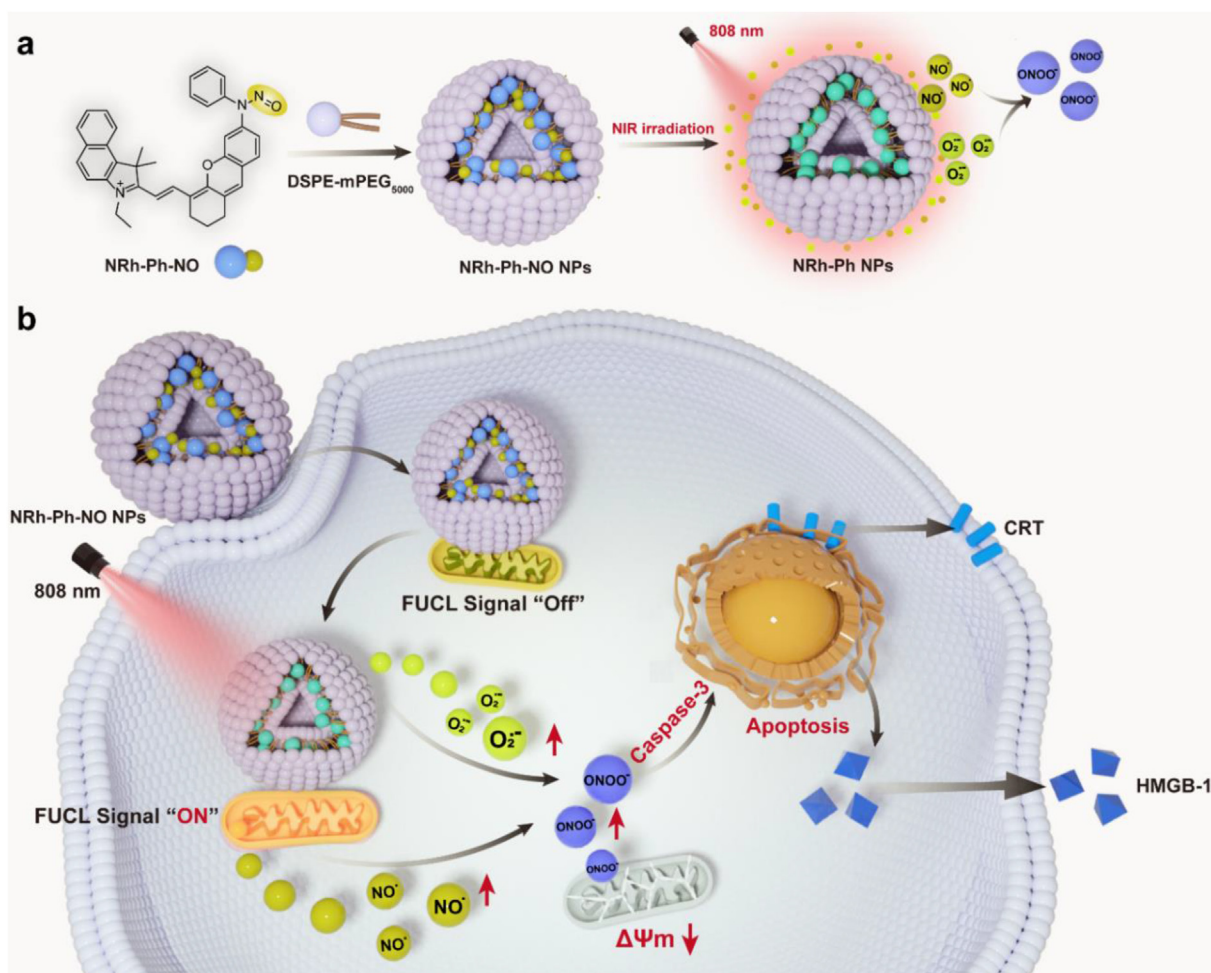
Gas therapy is a novel biomedical strategy that applies gaseous signal molecules, including nitric oxide (NO), carbonic oxide (CO), or sulfuretted hydrogen (H_2S), for the treatment of multiple diseases, especially cancer. It has the unique advantages of non-invasiveness, low systemic toxicity, and high selectivity^{1–6}. Extensive studies have indicated the mechanism of NO in biology and medicine^{7–9}. NO exhibits dose-related efficacy with high micromolar level of NO and tends to be involved in the diffusion-controlled reaction¹⁰. It reacts with oxygen molecules (O_2) and superoxide radicals ($O_2^{\cdot-}$) to form the much more powerful reactive oxygen/nitrogen species (ROS/RNS), such as $ONOO^-$, a key element in apoptosis of tumor cells^{11–19}. Hence, the strategy of RNS-mediated therapy may have great potential in cancer treatment. Additionally, since NO has gaseous properties of a high diffusion rate, short half-life, and minimal targeting efficiency²⁰, the accurate release of NO donors endowed with measurable spatial and temporal control is essential for the sustained efficacious gas therapy. Recently, it has been shown that organelle-targeted gas therapy can enhance therapeutic outcomes. Mitochondria are emerging as a new therapeutic target for amplified gas therapies due to their critical role in initiating endogenous apoptotic pathways. Therefore, *in situ* dynamic analysis of sub-cellular states during the treatment is important to elucidate the mechanisms involved and provides a new frontier for the next generation of gas therapy.

Numerous NO donors (*e.g.*, *N*-nitrosoamines, *N*-diazoniumdiolates, L-arginine, and *S*-nitrosothiols) are commonly employed for NO release, which can be readily tuned through a specific stimulus source, such as light, enzyme, pH, thermal source, and ultrasound^{21–29}. Among them, the light-triggered NO donors have been exploited due to their non-invasiveness, superior flexibility, high sensitivity, and precise spatiotemporal controllability^{30,31}. Despite the substantial progress, the existing light-controlled NO donors are mostly activated by visible light with potential phototoxicity³². Therefore, extending the toolbox of NO donors activated by longer wavelengths of near-infrared (NIR) light is important. The 808 nm near-infrared light is considered the most advantageous excitation source for *in vivo* phototherapy due to its relatively long wavelength with deeper-penetrating ability and low absorption of endogenous biomolecules and water

molecule in mammalian tissues^{33,34}. Given the limitations of UV–Vis light, 808 nm light-activated NO delivery is promising for improving the efficacy of NO-based cancer therapy, but challenges remain in the real-time visualization and *in situ* monitoring of NO release at the tumor site.

In the past few decades, extensive efforts have contributed to the advances in image-guided therapy. Among them, frequency upconversion luminescence (FUCL) has gained prominence in biosensing and imaging due to its superior properties of deep-tissue penetration, low autofluorescence, high photostability, and high signal-to-noise ratio. Furthermore, diverse FUCL-based systems have been extensively developed for detecting metal ions, tumor hypoxia, and cancer therapy^{35–41}. Recently, our group reported the design of 658 nm light-activable upconversion luminescent NO nano-prodrugs that facilitated precise real-time NO monitoring and tumor treatment guided by FUCL imaging⁴². However, the simultaneous organelle-specific NO release and FUCL imaging induced by an 808 nm laser have not been reported.

Herein we report the design, synthesis, and evaluation of a series of 808 nm photoactivatable rhodamine NO donors (NRh-R-NO, R = Me, Et, Bn, *i*Pr, and Ph) for spatio-selective controllable NO release for gas therapy guided by accurate FUCL imaging in mitochondria. Among these, *N*-nitrosoaniline-based NO donor NRh-Ph-NO exhibited low N–N bond dissociation energy (BDE), selectively releasing NO by 808 nm light stimulus and regulating the NO release rates. Significantly, the excited NRh-Ph-NO could release NO and generate the NRh-Ph molecule, which could trigger $O_2^{\cdot-}$ production with excellent PDT efficacy. Moreover, NIR light-released NO molecules could react with light-triggered ROS to generate RNS ($ONOO^-$) with strong anti-tumor activity through the cascade reaction. We chose liposome as an encapsulating matrix to maximize the gas therapeutic effect of NRh-Ph-NO and obtained the nanosystem NRh-Ph-NO NPs, which could be taken up into the mitochondria of tumor cells (see Scheme 1). Under the 808 nm laser irradiation, NRh-Ph-NO NPs could exert their cytotoxicity, cause a decrease in mitochondrial membrane potential, activate the caspase-3 pathway of apoptosis, and induce tumor immunogenic cell death. Our *in vivo* results validated the extraordinary performance of FUCL imaging-guided gas therapy for tumor eradication. Our study may open a new direction for achieving efficient photo-mediated gas treatment of cancer.



Scheme 1 (a) The construction of NRh-Ph-NO NPs. The nanogenerator NRh-Ph-NO NPs would be gradually activated by 808 nm laser to release NO and O_2^- and further produce highly toxic $ONOO^-$. (b) Schematic illustration of the nanogenerator NRh-Ph-NO NPs for *in vivo* NIR-light-initiated gas-mediated cancer therapy, allowing for simultaneous FUCL real-time imaging in mitochondria.

2. Materials and methods

2.1. Synthesis of NRh-R-NO

The synthesis method is universal. NRh-R (1 mmol, R = Me, Et, Bn, *i*Pr and Ph) and $NaNO_2$ (5 mmol) were dissolved in 2 mL DCM and 1 mL THF and stirred on ice bath for 5 min. Then the mixture was added dropwise with 400 μ L acetic acid. After completion, the excess amount of acetic acid was destroyed by saturated sodium bicarbonate solution. The organic layer was collected and washed with saturated sodium chloride solution. The crude product was concentrated and purified by silica gel column chromatography in DCM/MeOH (100:0 \rightarrow 100:1, *v/v*) to afford pure product NRh-R-NO.

NRh-Me-NO: 1H NMR (300 MHz, $CDCl_3$) δ 8.72 (d, $J = 15.1$ Hz, 1H), 8.23 (d, $J = 8.4$ Hz, 1H), 7.97 (dd, $J = 13.1$, 8.6 Hz, 2H), 7.72 (s, 1H), 7.69–7.62 (m, 1H), 7.60–7.48 (m, 2H), 7.42 (d, $J = 8.5$ Hz, 1H), 7.33 (d, $J = 8.5$ Hz, 1H), 7.05 (s, 1H), 6.65 (d, $J = 15.1$ Hz, 1H), 4.65 (d, $J = 6.3$ Hz, 2H), 3.49 (s, 3H), 2.86–2.57 (m, 4H), 2.03 (s, 6H), 2.00–1.96 (m, 2H), 1.55 (d, $J = 5.9$ Hz, 3H). ^{13}C NMR (75 MHz, $DMSO-d_6$) δ 174.41, 158.50, 144.45, 143.68, 138.57, 132.64, 131.05, 130.23, 129.04, 128.67, 128.54, 128.28, 127.10, 126.53, 122.82, 114.54, 105.80,

52.56, 45.04, 31.40, 31.10, 28.84, 26.92, 25.18, 23.74, 22.80, 19.88, 13.27. HRMS (ESI $^+$): Calcd. For $C_{32}H_{32}N_3O_2^+$ 490.2489 [M $^+$]; Found 490.2483.

NRh-Et-NO: 1H NMR (400 MHz, methanol- d_4) δ 8.92 (d, $J = 15.3$ Hz, 1H), 8.41 (d, $J = 8.5$ Hz, 1H), 8.16 (d, $J = 8.9$ Hz, 1H), 8.11 (d, $J = 3.1$ Hz, 1H), 7.84 (d, $J = 8.9$ Hz, 1H), 7.81 (s, 1H), 7.75 (dd, $J = 8.3$, 6.9 Hz, 1H), 7.65–7.61 (m, 2H), 7.54 (dd, $J = 8.5$, 2.1 Hz, 1H), 7.32 (s, 1H), 6.70 (d, $J = 15.3$ Hz, 1H), 4.60 (q, $J = 7.2$ Hz, 2H), 4.20 (d, $J = 7.1$ Hz, 2H), 2.83–2.77 (m, 4H), 2.11 (s, 6H), 1.98 (d, $J = 6.1$ Hz, 2H), 1.58 (s, 3H), 1.18 (s, 3H).

NRh-Bn-NO: 1H NMR (300 MHz, methanol- d_4) δ 8.76 (d, $J = 15.3$ Hz, 1H), 8.28 (d, $J = 8.4$ Hz, 1H), 8.07 (dd, $J = 13.7$, 8.5 Hz, 2H), 7.71 (d, $J = 8.7$ Hz, 2H), 7.55 (d, $J = 7.1$ Hz, 1H), 7.42 (dt, $J = 8.3$, 3.2 Hz, 4H), 7.30 (d, $J = 8.5$ Hz, 2H), 7.16 (s, 1H), 7.10 (d, $J = 2.1$ Hz, 1H), 7.04 (dd, $J = 8.6$, 2.2 Hz, 1H), 6.41 (d, $J = 14.6$ Hz, 1H), 4.61 (s, 2H), 4.43 (q, $J = 7.2$ Hz, 2H), 2.76 (dd, $J = 13.4$, 6.4 Hz, 4H), 2.03 (s, 6H), 1.52 (t, $J = 7.2$ Hz, 4H).

NRh-*i*Pr-NO: 1H NMR (300 MHz, $CDCl_3$) δ 8.77–8.63 (m, 1H), 8.17 (d, $J = 8.4$ Hz, 1H), 7.98 (dd, $J = 15.6$, 8.4 Hz, 2H), 7.78 (t, $J = 8.5$ Hz, 1H), 7.63 (d, $J = 7.3$ Hz, 1H), 7.54 (dd, $J = 17.1$, 9.0 Hz, 2H), 7.43 (d, $J = 8.2$ Hz, 1H), 7.35 (s, 1H), 7.15 (d, $J = 6.3$ Hz, 1H), 6.60 (d, $J = 15.3$ Hz, 1H), 4.60 (d,

$J = 7.1$ Hz, 2H), 3.87–3.76 (m, 1H), 2.75 (d, $J = 17.5$ Hz, 4H), 2.02 (s, 6H), 1.91–1.85 (m, 2H), 1.56 (s, 3H), 1.26 (d, $J = 6.9$ Hz, 6H). ^{13}C NMR (75 MHz, DMSO) δ 179.44, 158.07, 152.34, 144.62, 141.06, 132.70, 132.64, 131.03, 129.57, 128.98, 128.23, 127.06, 123.27, 122.74, 121.96, 114.54, 112.63, 110.46, 67.07, 52.57, 47.17, 44.94, 34.14, 28.87, 27.67, 27.64, 26.80, 25.18, 23.66, 21.91, 19.30, 13.26, 13.02. HRMS (ESI⁺): Calcd. For $\text{C}_{34}\text{H}_{36}\text{N}_3\text{O}_2^+$ 518.2802 [M^+]; Found 518.2800.

NRh-Ph-NO: ^1H NMR (300 MHz, CDCl_3) δ 8.79 (d, $J = 15.2$ Hz, 1H), 8.26 (d, $J = 8.7$ Hz, 1H), 8.06 (dd, $J = 12.1$, 8.8 Hz, 3H), 7.86 (d, $J = 1.9$ Hz, 1H), 7.74 (d, $J = 7.2$ Hz, 1H), 7.66 (d, $J = 10.8$ Hz, 2H), 7.59 (d, $J = 7.8$ Hz, 3H), 7.34 (d, $J = 8.4$ Hz, 1H), 7.14–7.08 (m, 3H), 6.79 (dd, $J = 8.5$, 2.1 Hz, 1H), 4.83–4.73 (m, 2H), 2.90 (t, $J = 4.3$ Hz, 2H), 2.80–2.75 (m, 2H), 2.10 (s, 6H), 2.06 (s, 2H), 1.63 (d, $J = 2.7$ Hz, 3H). ^{13}C NMR (75 MHz, DMSO) δ 158.31, 152.77, 143.67, 138.99, 138.56, 138.46, 135.88, 130.18, 130.02, 129.91, 129.77, 129.54, 128.93, 128.83, 127.73, 127.01, 126.37, 123.22, 122.83, 122.75, 122.69, 121.93, 120.45, 119.82, 114.46, 110.43, 105.94, 52.54, 44.88, 34.09, 26.81, 26.69, 23.63, 13.18, 13.03. HRMS (ESI⁺): Calcd. For $\text{C}_{37}\text{H}_{34}\text{N}_3\text{O}_2^+$ 552.2646 [M^+]; Found 552.2733.

2.2. Other protocols

Synthesis and characterization of Me, *i*Pr and NRh-R, spectroscopic methods, phototriggered and control release assay, selectivity assays, preparation and characteristics of NRh-Ph-NO NPs, *in vitro* NO, ROS and ONOO⁻ detection, intracellular ROS, NO and ONOO⁻ detection, MTT assay, Calcein-AM/PI staining assay, flow cytometer assay, mitochondrial membrane potential detection, western blotting, immunogenic cell death (ICD) biomarkers detection, *in vivo* imaging, *in vivo* anti-tumor activity and histological analyses were presented in Supporting Information.

3. Results and discussion

3.1. Synthesis, characterization, and upconversion properties of NRh dyes and NO donors

Based on the FUCL properties of the reported rhodamine scaffold, we introduced different substituents (methyl, ethyl, benzyl, isopropyl, and phenyl) to the parent nucleus to synthesize a series of rhodamine derivatives NRh-R (R = Me, Et, Bn, *i*Pr and Ph) (Supporting Information Schemes S1 and S2, Figs. S1–S15). The precursors NRh-R were prepared according to the previously reported method, and further details are provided in the Supporting Information. The schematic of NRh-R-NO synthesis is outlined in Fig. 1a. Typically, the desired final products, *N*-nitrosated compounds NRh-R-NO, were obtained by nitrosation with NaNO_2 , and their structures were confirmed by ^1H NMR, ^{13}C NMR, and high-resolution mass spectra (Supporting Information Figs. S16–S26).

The optical properties of NRh-R and NRh-R-NO (R = Me, Et, Bn, *i*Pr and Ph) were characterized and are presented in Fig. 1 and Supporting Information Figs. S27–S29. After nitrosation, the maximum absorption peaks of NRh-R-NO showed a blue shift from 720 nm to around 600 nm (Fig. 1c). The upconversion luminescence of NRh-R-NO exhibited faint emission compared to the NRh-R precursor (Fig. 1d). These results were mainly ascribed to the electron-withdrawing property of the *N*-nitrosated group. The FUCL properties generated by the NRh-R dyes were verified by their FUCL behaviors in the methanol solvent system. As the

temperature increased from 0 to 40 °C, the NRh-R absorbance gradually decreased (Supporting Information Fig. S27). By contrast, after 808 nm laser irradiation, the FUCL intensities of NRh-R were enhanced (Fig. 1e and Supporting Information Fig. S28). Besides, with the increase of laser power density, the anti-Stokes emission at 740 nm was gradually increased in a linear relationship, substantiating that the exciton process was due to the hot-band absorption-assisted single photon process (Fig. 1f and Supporting Information Fig. S29)⁴³.

3.2. 808 nm-triggered and controlled release properties of NO donors

The solutions of different NO donors were irradiated with an 808 nm laser and investigated by absorption and FUCL spectra to assess the photo-uncaging efficiency of NRh-R-NO (R = Me, Et, Bn, *i*Pr, and Ph). Interestingly, only NRh-Ph-NO could be triggered by an 808 nm laser compared with other NO donors. As depicted in Fig. 2a–d, the maximum absorption of NRh-Ph-NO at 580 nm and 620 nm was gradually decreased, accompanied by the increased characteristic absorption peak of NRh-Ph at 720 nm. Besides, the FUCL signal of NRh-Ph at 740 nm was significantly enhanced with the extended irradiation time. In contrast, the absorption and FUCL spectra intensities of NRh-R-NO (R = Me, Et, Bn, *i*Pr) were almost unchanged (Supporting Information Fig. S30). These results indicated that when stimulated by an 808 nm laser, only NRh-Ph-NO could be decomposed into the NO uncaging FUCL dye NRh-Ph. Thus, further investigation for precise NO release controllability is clearly warranted for *in vivo* gas therapy.

The NO uncaging process of NRh-Ph-NO was monitored by the fluorescence response, as the NRh-Ph-NO could be alternately activated and deactivated by periodically adjusting the 808 nm NIR irradiation light on and off (Fig. 2e). Only an external stimulus, like 808 nm light, could induce NO release, making the spatiotemporal-specific controllability of NO release feasible (Fig. 2f). The NO release was also quantified by Griess assay (Supporting Information Fig. S31). In addition, density functional theory (DFT) calculation was performed to unravel why only phenyl-substituted NO donors could be released (Fig. 2g). The results showed that the N–N bond dissociation energies (BDE) of NRh-R-NO (R = Me, Et, Bn, *i*Pr and Ph) were 39.4, 38.9, 38.9, 39.4, and 30.4 kcal/mol, respectively. The NO release from NRh-Ph-NO was easier than those from the other NO donors, consistent with the previous experimental data, indicating that NRh-Ph-NO was a potential NO donor candidate for 808 nm light-activatable biological application *in vivo*²⁴.

3.3. 808 nm-triggered NO-uncaging mechanism and RONS detection of NRh-Ph-NO

The schematic diagram of ROS/RNS generation pathways is illustrated in Fig. 3a. The photolysis of phenyl-substituted *N*-nitrosamine undergoes a reactive intermediate containing the positively charged divalent nitrogen atom while releasing NO. The NO release and NO• generation by the photolysis of NRh-Ph-NO were investigated by fluorescence and electron spin resonance (ESR) spectra, using RhBs as the NO indicator and 2-phenyl-4,4,5,5-tetramethylimidazole-1-oxyl 3-oxide (PTIO radical) as a spin trapper^{44,45}. With extended 808 nm light irradiation, the characteristic peaks of RhB and the PTIO signal gradually enhanced, indicating that NRh-Ph-NO possessed efficient light-

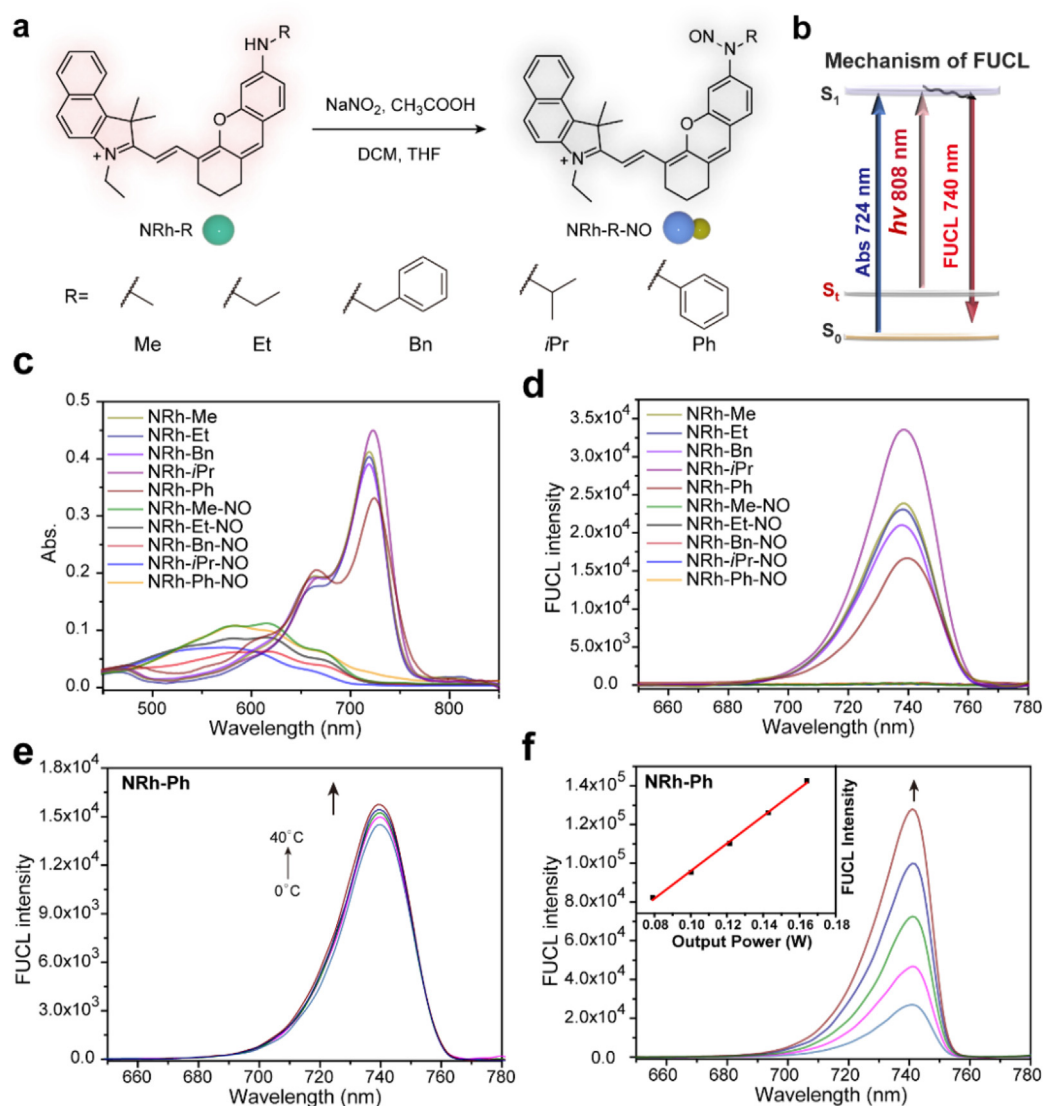


Figure 1 (a) Synthetic route of *N*-nitrosated compounds NRh-R-NO (R = Me, Et, Bn, *i*Pr and Ph). (b) Schematic illustration of the mechanism of frequency upconversion luminescence (FUCL) in NRh-Ph. (c) Absorbance and (d) FUCL spectra of NRh-R and NRh-R-NO (R = Me, Et, Bn, *i*Pr and Ph) (5 μmol/L) in methanol, Ex = 808 nm. (e) FUCL properties of NRh-Ph (5 μmol/L) in methanol, λ_{exc} = 808 nm. (f) Linear relationship between FUCL intensity and different power density of 808 nm laser in NRh-Ph solution (5 μmol/L).

controlled release ability to induce NO uncaging and NO generation (Fig. 3b–d and Supporting Information Fig. S32). During the NO release process, the excited NRh-Ph-NO system could generate NRh-Ph molecules, triggering O₂^{•-} production activated by the 808 nm laser for the NIR-enhanced PDT effect. Therefore, dihydrorhodamine 123 (DHR 123) was utilized for monitoring O₂^{•-} generation and to determine whether NRh-Ph-NO could enhance NIR-catalysis (Fig. 3e and f, and Supporting Information Fig. S33). After mixing NRh-Ph-NO with the DHR 123 probe, the fluorescence spectra were collected at 14 min after 808 nm irradiation. Upon exposure to 808 nm irradiation, the characteristic peak of DHR 123 at 526 nm showed a significant increase, indicating effective O₂^{•-} generation. Besides, the ESR experiment was conducted to detect O₂^{•-} generation during photolysis. The O₂^{•-} levels in the NRh-Ph-NO combined with the NIR light irradiation exhibited a significant increase (Fig. 3g), further confirming that

NRh-Ph-NO could serve as a potential photosensitizer to generate O₂^{•-}. Additionally, upon 808 nm light irradiation, a nonradical substance, photogenerated ONOO⁻ in NRh-Ph-NO solution, was detected by an ONOO⁻-specific probe reported by Yoon et al.⁴⁶ based on the fluorescence change. The fluorescence fluctuation was positively related to the generation of NO and O₂^{•-} (Fig. 3h and i, and Supporting Information Fig. S34). The photophysical mechanism of the process of NO uncaging from NRh-Ph-NO with DFT was executed using Gaussian 16 at the B3LYP/6-311G(d) level of theory (Fig. 3j)^{47,48}. The N–NO bond brought π-electrons and structural effects on the –NH(Ph) substituent, facilitating the intramolecular charge transfer (ICT) process, causing blue-shift of absorption, consistent with previous results²⁵. Taken together, the NRh-Ph-NO system could achieve triple amplification of the tumor gas therapy by releasing NO activated by 808 nm and converting NO into NO•, NRh-Ph-induced ROS

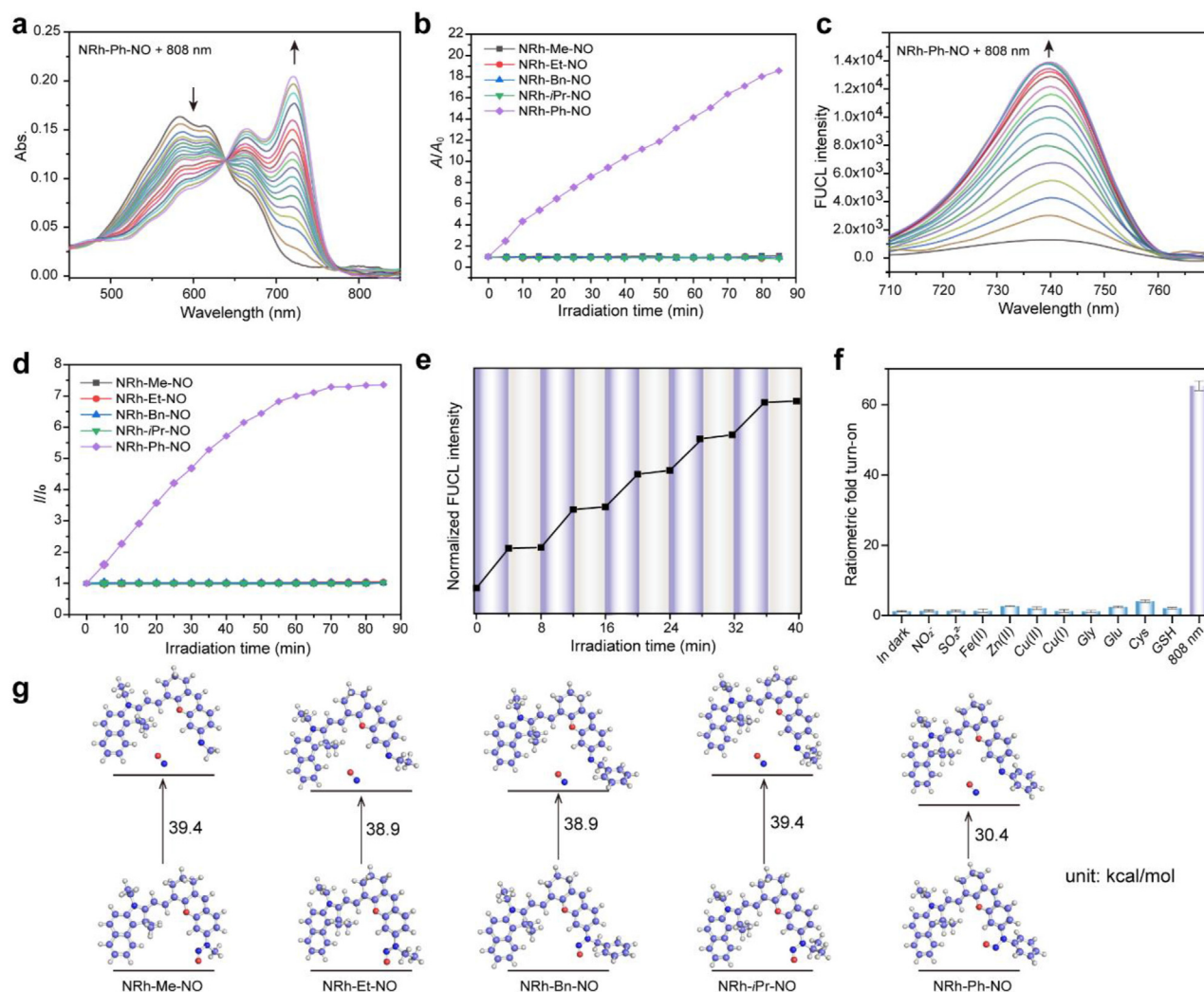


Figure 2 Photo-triggered and controlled release of NRh-Ph-NO. (a, b) Absorption spectra of the photolysis of NRh-R-NO upon 808 nm light irradiation. (c, d) FUCI spectra of the photolysis of NRh-R-NO upon NIR light irradiation, $\lambda_{\text{ex}} = 808 \text{ nm}$. (e) The NIR-photolysis controllability of NRh-Ph-NO ($\text{Abs}_{620 \text{ nm}} = 0.15$) by adjusting light “on” (purple) and “off” (grey). (f) Ratiometric turn-on fold of NRh-Ph-NO ($5 \mu\text{mol/L}$) upon exposure to redox mental ($200 \mu\text{mol/L}$), amino acids (1 mmol/L) and irradiated at NIR light ($n = 3$). (g) The N–N bond dissociation energy (BDE) of different compounds.

generation and ONOO^- production to improve RNS-mediated cancer therapy.

3.4. Preparation and characterization of nanogenerator NRh-Ph-NO NPs

Encouraged by the excellent NIR photo response performance and reactive nitrogen production capacity of NRh-Ph-NO, we prepared NRh-Ph-NO NPs *via* biodegradable DSPE-mPEG₅₀₀₀-assisted encapsulation of NRh-Ph-NO for *in vivo* application (Fig. 4a). The dynamic light scattering (DLS) and transmission electron microscopy (TEM) analyses indicated that NRh-Ph-NO NPs were of spherical morphology that could readily disperse in the aqueous solution with a hydrodynamic size of $\approx 48 \text{ nm}$

(Fig. 4b). The response of NRh-Ph-NO NPs toward NIR light was investigated by monitoring the UV–Vis/NIR absorption and FUCI signals upon continuous 808 nm laser treatment. As with the 808 nm irradiation, the absorbance of NRh-Ph-NO NPs at around 600 nm gradually decreased, while the NIR absorption at 720 nm increased (Fig. 4c). Consequently, the FUCI signal of NRh-Ph-NO NPs at 740 nm was significantly enhanced (Fig. 4d). We also evaluated the RNS generation ability of NRh-Ph-NO NPs. Upon addition of specific ONOO^- probe PNAP, the fluorescence intensity at 640 nm gradually increased with prolonged 808 nm laser irradiation time, confirming the ONOO^- production (Fig. 4e). Moreover, the controllability was detected with CCD imaging with the letters “CPU” on filter paper, which could optionally light up one

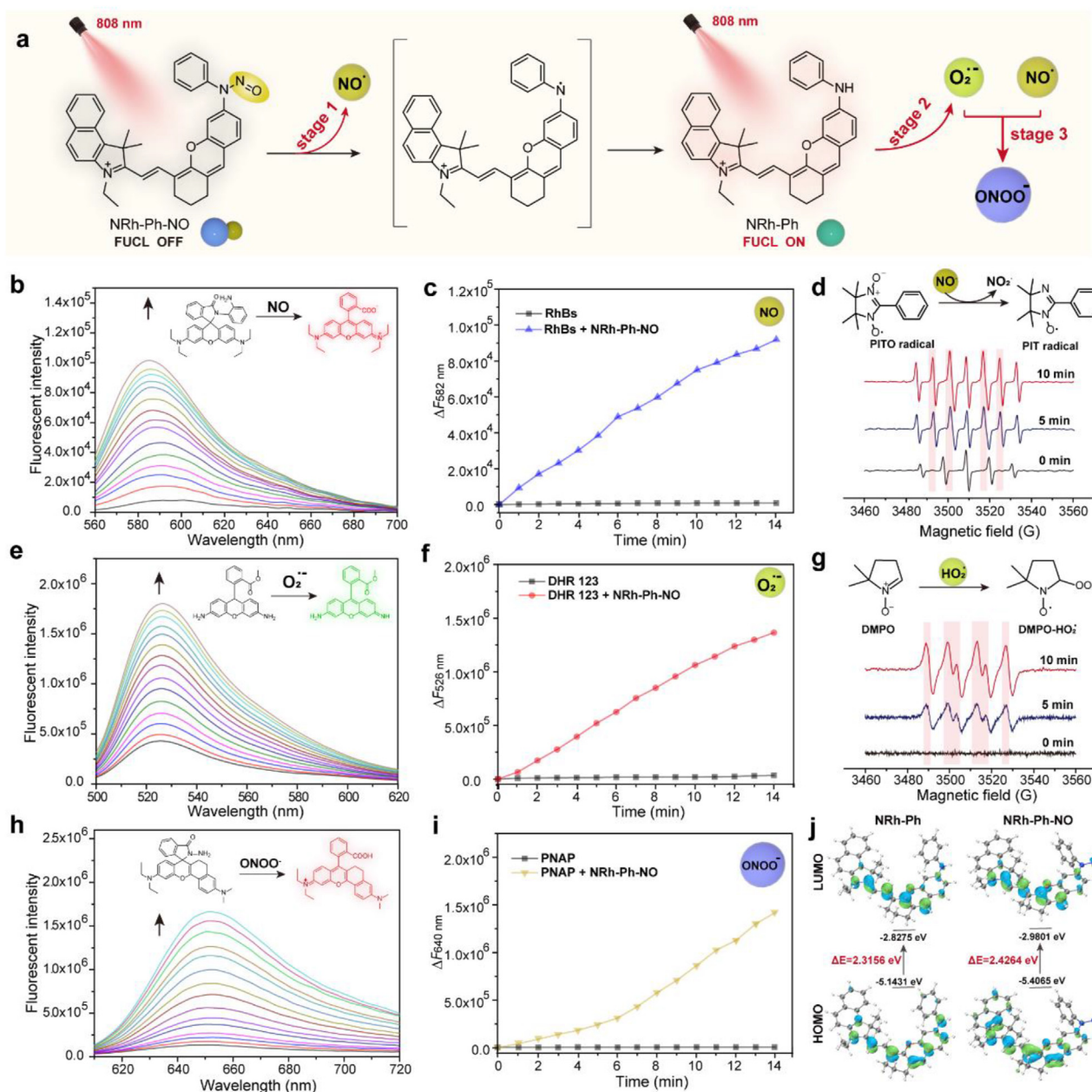


Figure 3 (a) Schematic illustrations of the NIR photolysis performance of NRh-Ph-NO for RNS generation. (b, c) The NO release of 5 $\mu\text{mol/L}$ NRh-Ph-NO in MeOH/H₂O (2:1, v/v) under 808 nm irradiation, using RhBs as NO indicator (10 $\mu\text{mol/L}$, $\lambda_{\text{em}} = 582 \text{ nm}$) (d) ESR spectra demonstrating NO \cdot generation from NRh-Ph-NO triggered by 808 nm. (e, f) The O₂ \cdot^- generation from 5 $\mu\text{mol/L}$ NRh-Ph-NO in MeOH/H₂O (2:1, v/v) triggered by 808 nm, using DHR 123 as O₂ \cdot^- indicator (5 $\mu\text{mol/L}$, $\lambda_{\text{em}} = 526 \text{ nm}$) (g) ESR spectra demonstrating O₂ \cdot^- generation from NRh-Ph-NO triggered by 808 nm. (h, i) The ONOO \cdot^- production of 5 $\mu\text{mol/L}$ NRh-Ph-NO in MeOH under 808 nm irradiation, using PNAP as ONOO \cdot^- probe (15 $\mu\text{mol/L}$, $\lambda_{\text{em}} = 640 \text{ nm}$) (j) The major contributing HOMO and LUMO orbitals of ground state NRh-Ph-NO and NRh-Ph.

letter at a time (Fig. 4f). Hence, the nanogenerator was expected to strictly adhere to the NIR light activation and verify the spatiotemporal gas release with FUCL monitoring. The results revealed that the response of NRh-Ph-NO NPs to NIR light in an aqueous solution afforded an “off-on” FUCL signal and potential ONOO \cdot^- generation capabilities.

3.5. *In vitro* cellular gas therapy based on 808 nm-excited NRh-Ph-NO NPs

The light-controlled release capability and photolysis visualization are important for effective delivery of nanogenerators into cancer cells to achieve high therapeutic efficacy. 4T1 cells were

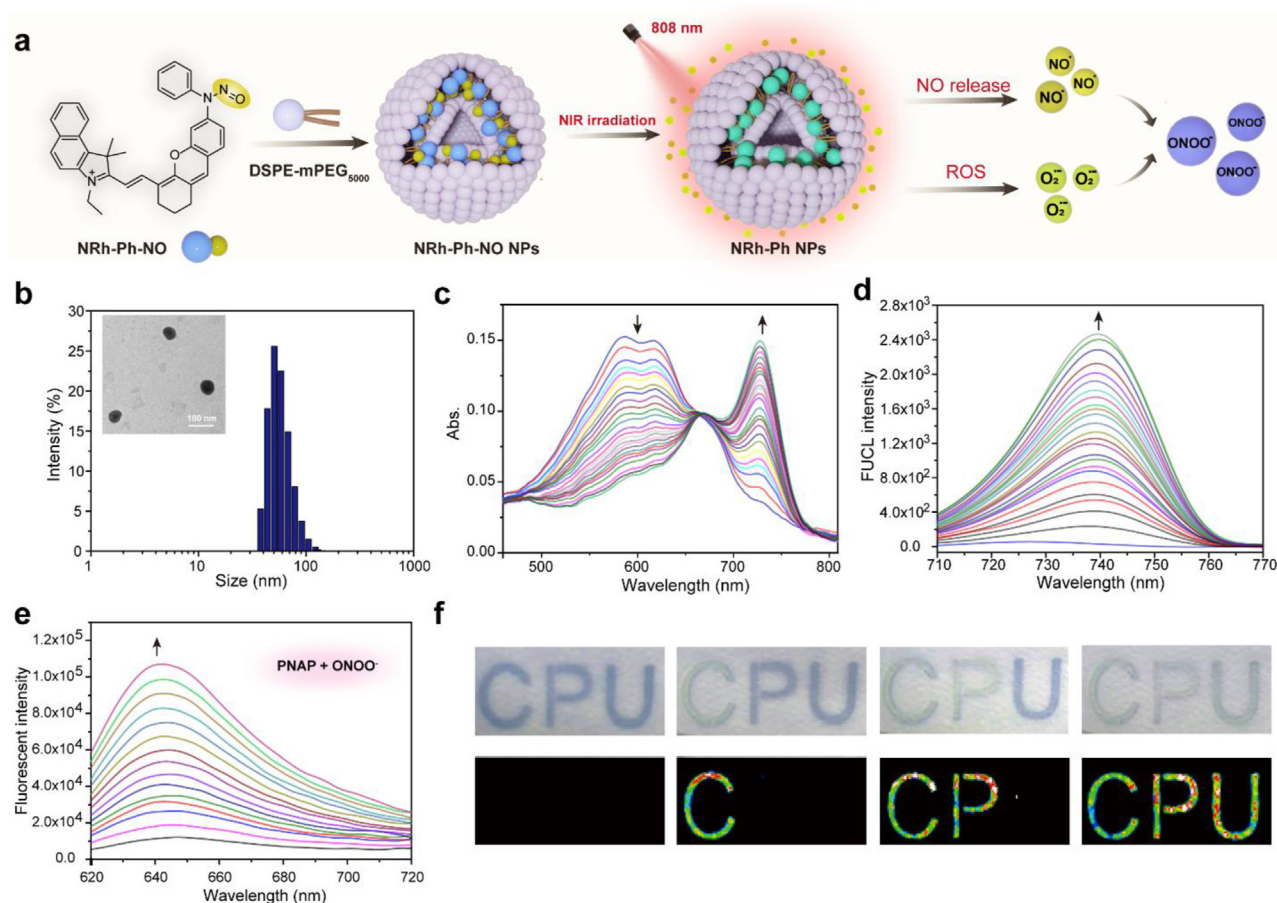


Figure 4 Characterization of NRh-Ph-NO NPs nanoparticles. (a) The construction of NRh-Ph-NO NPs and photolysis scheme of NRh-Ph-NO NPs. (b) DLS of NRh-Ph-NO NPs nanoparticles. Insert: TEM image of NRh-Ph-NO NPs. (c) UV-Vis and (d) FUCI spectra of NRh-Ph-NO NPs photolysis upon 808 nm light irradiation, $\lambda_{\text{ex}} = 808$ nm. (e) The ONOO⁻ production of NRh-Ph-NO NPs under 808 nm irradiation, using PNAP as ONOO⁻ probe. (f) CCD image of selective light-activation from NRh-Ph-NO NPs in filter paper.

incubated with NRh-Ph-NO NPs and specific NO indicator probe RhBs to verify the NIR light-controlled photolysis of NRh-Ph-NO NPs in cancer cells. As shown in Fig. 5a, negligible FUCI and NO indicator probe fluorescence signals were observed for NRh-Ph-NO NPs-treated cells without laser irradiation. When the 808 nm irradiation elapsed, NRh-Ph-NO NPs could gradually light up and trigger NO release with the enhancement of red fluorescence from NRh-Ph and green fluorescence from NO indicator probe RhBs, indicating the controllability of NIR light activation. Furthermore, to corroborate whether the process originated from mitochondria, MitoTracker[®] probe Rh123 was used to label mitochondria in 4T1 cells. As displayed in Fig. 5b, a faint fluorescence signal was observed for NRh-Ph-NO NPs-treated cells without laser irradiation. In contrast, an intracellular fluorescence signal was observed upon laser irradiation, and the pattern of NRh-Ph FUCI signal overlapped with Mito Tracker Rh123 (Fig. 5b), confirming the specific photolysis of NRh-Ph-NO NPs in mitochondria. Next, the intracellular RONS level of NRh-Ph-NO NPs was assessed using fluorescent probes DHE and PNAP for O₂⁻ and ONOO⁻ detection, respectively^{49,50}. Fig. 5c and d showed

that NRh-Ph-NO NPs-treated cells following 808 nm irradiation had much stronger green fluorescence than the control group, demonstrating higher RNS production.

Having validated NIR light-induced gas cascade reaction in mitochondria, we explored the synergistic effect on mitochondrial damage. NO and ROS/RNS could change the mitochondrial membrane potential ($\Delta\Psi_m$), leading to cell apoptosis. Mitochondrial membrane potential assay kit JC-1 was used to detect $\Delta\Psi_m$ changes. JC-1 accumulates in the aggregate form in the mitochondrial matrix of live cells with higher $\Delta\Psi_m$ and is dispersed in the monomer form in the cytosol of apoptotic cells with lower $\Delta\Psi_m$ ⁵¹. Fig. 5e showed that with increasing irradiation time, the green fluorescence intensities of 4T1 cells treated with NRh-Ph-NO NPs were gradually increased with the enhancement of the NIR channel signal. These results verified that NRh-Ph-NO NPs were capable of real-time monitoring the NO release in mitochondria and could potentially trigger the combined effect of RNS and damage the critical mitochondrial membrane after photolysis.

Given the cascade response of NRh-Ph-NO NPs under 808 nm laser stimulation, the biocompatibility and antitumor effect of

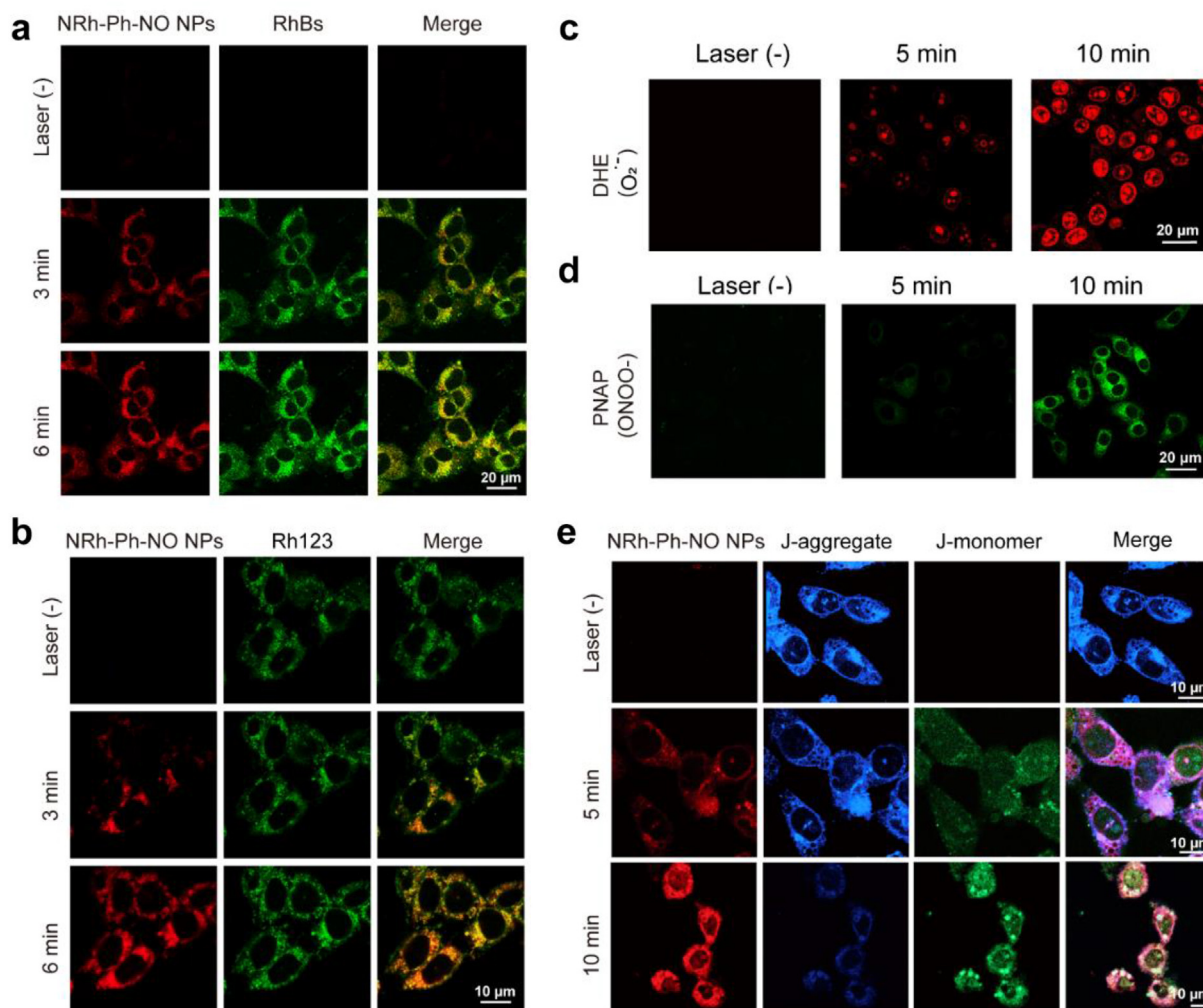


Figure 5 (a) CLSM images of NO release from NRh-Ph-NO NPs (red) in 4T1 cells co-incubated with NO indicator RhBs (green) with NIR photoirradiation (808 nm, 0.5 W/cm²). (b) CLSM images of 4T1 cells incubated with NRh-Ph-NO NPs (red) and mitochondria (green). Fluorescence images of (c) O₂⁻ and (d) ONOO⁻ generation from NRh-Ph-NO NPs in 4T1 cells with or without NIR photoirradiation. (e) Fluorescence images of mitochondrial membrane potential analyzed by JC-1.

nanogenerators *in vitro* were investigated by MTT assay (Supporting Information Fig. S35). The viability of 4T1 cells, incubated with various concentrations of NRh-Ph-NO NPs for 24 h, was still above 85%, indicating that nanogenerators possessed high biocompatibility. Fig. S8 showed that the survival rate of 4T1 cells was decreased to 27% when stimulated by 808 nm excitation, demonstrating that NRh-Ph-NO NPs with 808 nm light irradiation could effectively inhibit cancer cell growth. The anticancer effect of photocatalysis gas therapy *in vitro* was further investigated in 4T1 cells by calcein-AM (AM)/propidium iodide (PI) co-staining and flow cytometry by the Annexin V-FITC/PI apoptosis assay kit (Fig. 6a and b). Based on the live/dead staining assay, distinct red fluorescence was noticed in cells treated with NRh-Ph-NO NPs and 808 nm light, indicating significant cytotoxicity toward cancer cells. The percentages of apoptotic 4T1 cells treated with NRh-Ph-NO NPs without or with 808 nm laser irradiation for 5 and 10 min were 0.43%, 22.1% and 42.9%, respectively, demonstrating that NRh-Ph-NO NPs could regulate apoptosis and exert therapeutic effect with NIR light irradiation.

Subsequently, the cell death pathway and the mechanism of NRh-Ph-NO NPs in 4T1 cells were examined by Western blotting. As displayed in Fig. 6c and d, compared to other groups, the apoptosis-related cleaved caspase-3 in the NRh-Ph-NO NPs with 808 nm laser irradiation group was significantly up-regulated by the production of RNS, resulting in mitochondrial damage and cell death⁵². Similar results were obtained by AM/PI and flow cytometry analyses of apoptosis. These data confirmed that the NRh-Ph-NO NPs with 808 nm light resulted in significant cell apoptosis by increasing the cleaved caspase-3 level.

It has been shown that the damage-related molecular patterns (DAMPs), including calreticulin (CRT) and high mobility group box 1 (HMGB-1), may be released by dead tumor cells during immunogenic cell death (ICD)³. Therefore, we examined the CRT secretion and HMGB1 release from 4T1 cancer cells by immunofluorescence staining to verify whether NIR-triggered gas treatment led to ICD in addition to the direct killing of cancer cells. As shown in Fig. 6e, the surface-exposed CRT level in NRh-Ph-NO NPs-treated cells with prolonged 808 nm laser irradiation

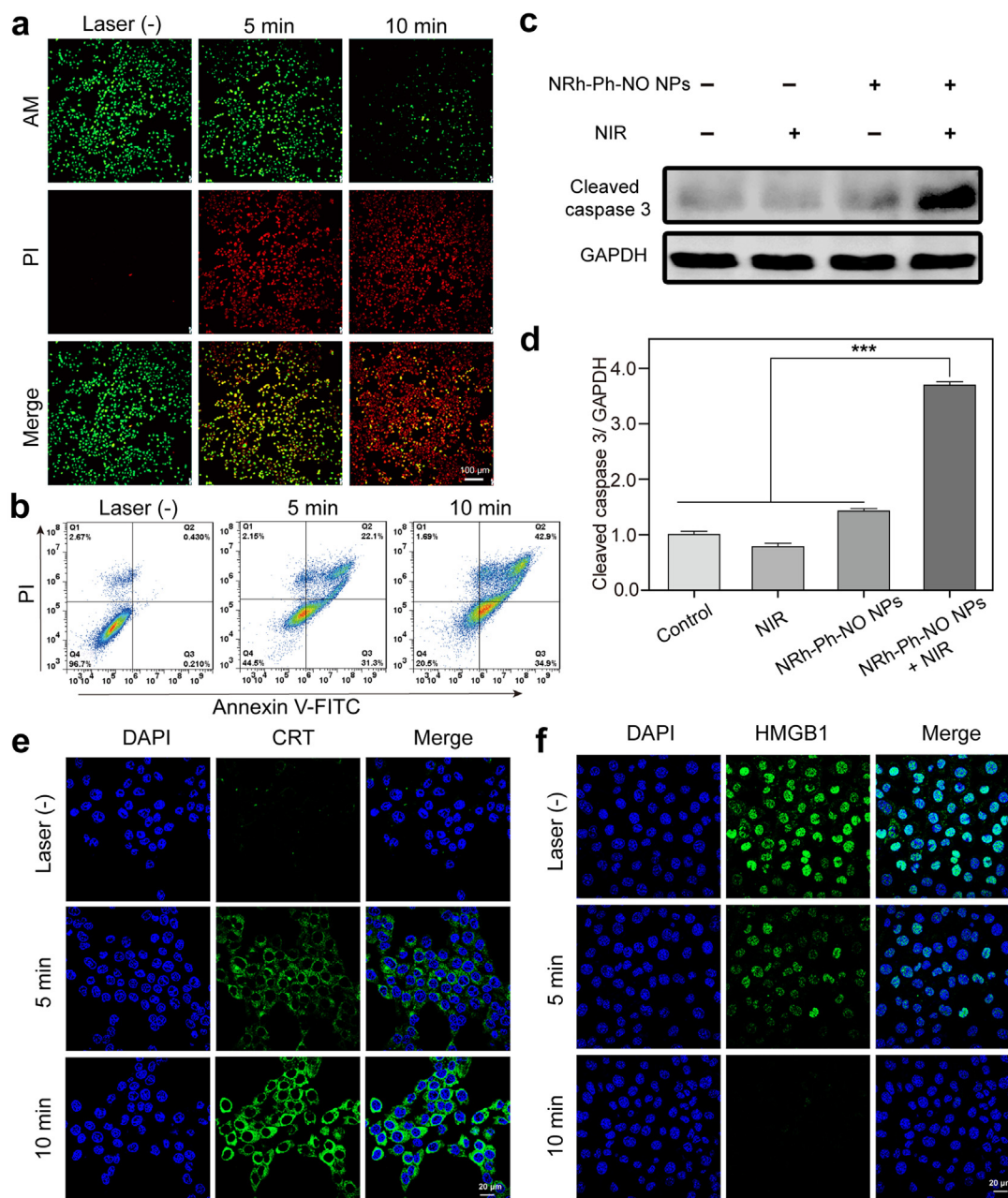


Figure 6 *In vitro* antitumor efficacy. (a) Fluorescence images of 4T1 cells co-incubated by Calcein-AM (green channel, live cells) and PI (red channel, dead cells) with NIR photoirradiation (808 nm, 0.5 W/cm²). Scale bar: 100 µm with NO indicator RhBs (green). Scale bar: 100 µm. (b) Apoptosis analysis of 4T1 cells with NRh-Ph-NO NPs with NIR photoirradiation (808 nm, 0.5 W/cm²). (c, d) Protein expression levels of cleaved caspase-3 measured by Western blotting in 4T1 cells (*n* = 3). Lane 1: control; Lane 2: NIR; Lane 3: NRh-Ph-NO NPs; Lane 4: NRh-Ph-NO NPs + NIR. Immunofluorescent images of (e) calreticulin and (f) high mobility group protein 1 in 4T1 cells treated with NRh-Ph-NO NPs under NIR photoirradiation (808 nm, 0.5 W/cm²). Scale bar: 20 µm.

was significantly higher than that in non-laser irradiated cells. Besides, the efficient release of HMGB-1 was observed by NRh-Ph-NO NPs plus NIR irradiation (Fig. 6f). These findings indicated that NIR-induced gas therapy could effectively induce ICD and release DAMPs from 4T1 cancer cells. The high levels of CRT expression and HMGB1 release from cancer cells following NRh-Ph-NO NPs treatment contributed to the activation of anti-tumor immunity and improved anticancer effect.

3.6. *In vivo* tumor imaging and photo-controlled NO release

In vivo bioimaging plays a crucial role in the accurate diagnosis and therapy of tumors. The light controllability of the nanogenerators also directly determines the gas release sites, which, in turn, impacts the effectiveness of gas treatment. Specifically, the nanogenerators can produce photolytic products with the turn-on FUCL signal under NIR light irradiation, providing higher resolution and sensitive real-

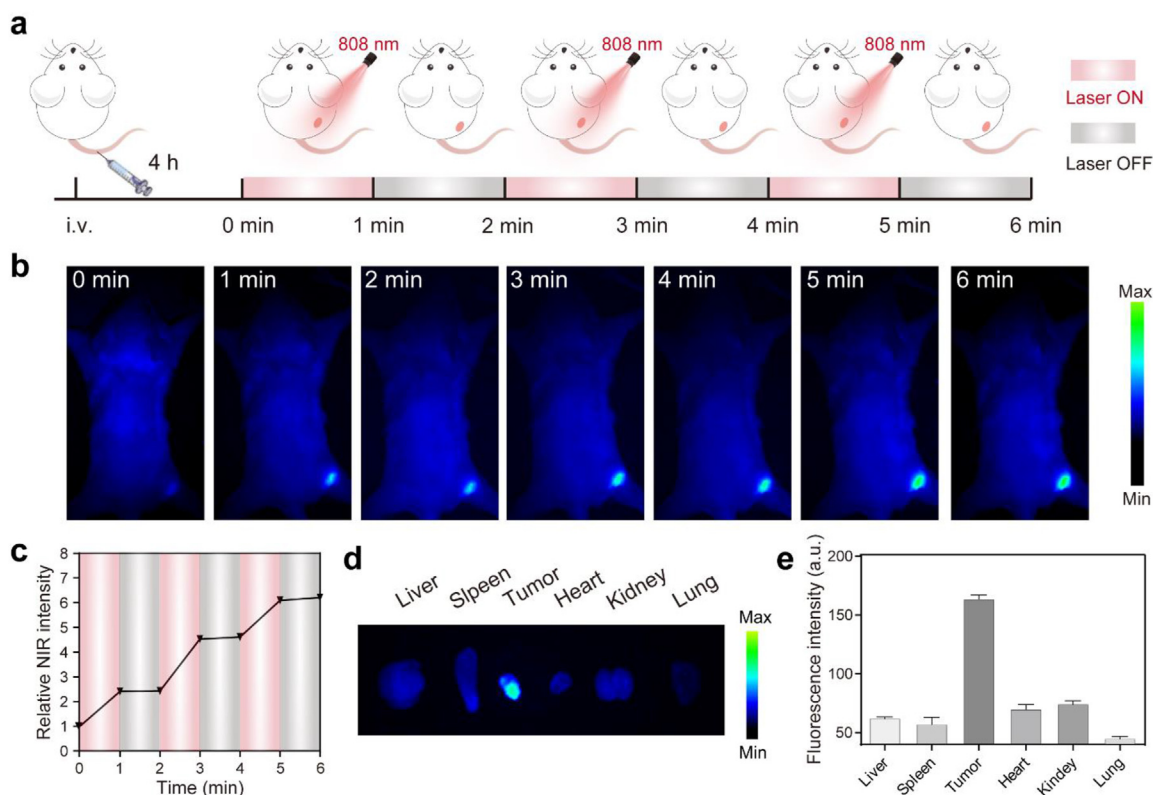


Figure 7 *In vivo* imaging of tumor-bearing mice with NRh-Ph-NO NPs. (a) *In vivo* imaging schedule of NRh-Ph-NO NPs. (b) *In vivo* CCD imaging of tumor-bearing mice after the tumor site was subjected to NIR light irradiation 4 h post i.v. injection of NRh-Ph-NO NPs. (c) Fluorescence ratio of the tumor site. (d) *Ex vivo* CCD imaging of major organs in tumor-bearing mice after the tumor site was subjected to NIR light irradiation 4 h post i.v. injection of NRh-Ph-NO NPs. (e) Fluorescence intensity of the major organs. Data are presented as mean \pm SD, $n = 3$.

time FUCL readout for *in vivo* monitoring. We investigated the tumor site accumulation and light-responsive properties of nanogenerator NRh-Ph-NO NPs in 4T1 tumor-bearing mice by detecting the FUCL signal. Detailed light-controlled release regimens of the bioimaging monitoring procedure are shown in Fig. 7a. After 1 min of 808 nm laser irradiation, a significant turn-on FUCL signal was observed. With increasing irradiation time, the FUCL signal of NRh-Ph-NO NPs became stronger at the tumor site and remained essentially unchanged when the laser was turned off (Fig. 7b–e and Supporting Information Fig. S36). The results demonstrated that NRh-Ph-NO NPs could effectively accumulate at the targeted tumor site, achieving controlled spatiotemporal NO release under 808 nm laser irradiation, crucial for their *in vivo* application.

3.7. *In vivo* anticancer effect of NRh-Ph-NO NPs

The *in vivo* anticancer effect of NRh-Ph-NO NPs with 808 nm laser irradiation was evaluated on 4T1 tumor-bearing mice (Fig. 8a). The mice were treated with saline, NRh-Ph-NO NPs, 808 nm laser irradiation, or NRh-Ph-NO NPs + 808 nm laser irradiation, respectively. The tumor sites were irradiated with 808 nm NIR of 0.8 W/cm² for 10 min at 4 h post-injection of NRh-Ph-NO NPs (5 mg/kg, 100 μ L). The tumor growth and body weight were measured every 2 days and monitored during the 14-day treatment period. As shown in Fig. 8b, tumor volumes of the mice treated with saline, NRh-Ph-NO NPs, or 808 nm laser

irradiation increased rapidly during treatment, which caused nearly no anticancer effects. In contrast, mice treated with NRh-Ph-NO NPs + 808 nm laser exhibited prominent tumor inhibition, indicating that 808 nm induced anticancer gas therapy effects. Importantly, no significant body weight variation was observed during the treatment (Fig. 8c). Also, no significant difference was found between all groups of mice, including the group injected intravenously with NRh-Ph-NO NPs, by the hematoxylin and eosin (H&E) staining of major organs, indicating the favorable biocompatibility and biosafety of NRh-Ph-NO NPs (Supporting Information Fig. S37). Additionally, H&E staining of the tumors showed that nanogenerators NRh-Ph-NO NPs caused damage to tumor cells. Furthermore, the caspase-3 immunofluorescence assay exhibited that NRh-Ph-NO NPs + NIR group had an increased level of the apoptosis biomarker caspase-3 in the tumors. Similar trends were also observed by substantial CRT protein exposure on the tumor cell surface, mainly attributed to the RNS-induced activated systemic antitumor immune response. The TUNEL staining assay presented that cell apoptosis levels were significantly upregulated in tumor tissues of mice treated with NRh-Ph-NO NPs + 808 nm laser compared with that of other groups, indicating the impressive therapeutic effect of NRh-Ph-NO NPs + NIR on eradicating solid tumors (Fig. 8d). Overall, nanogenerators NRh-Ph-NO NPs could synergistically orchestrate gas therapy and PDT, potentially amplifying anticancer therapeutic outcomes.

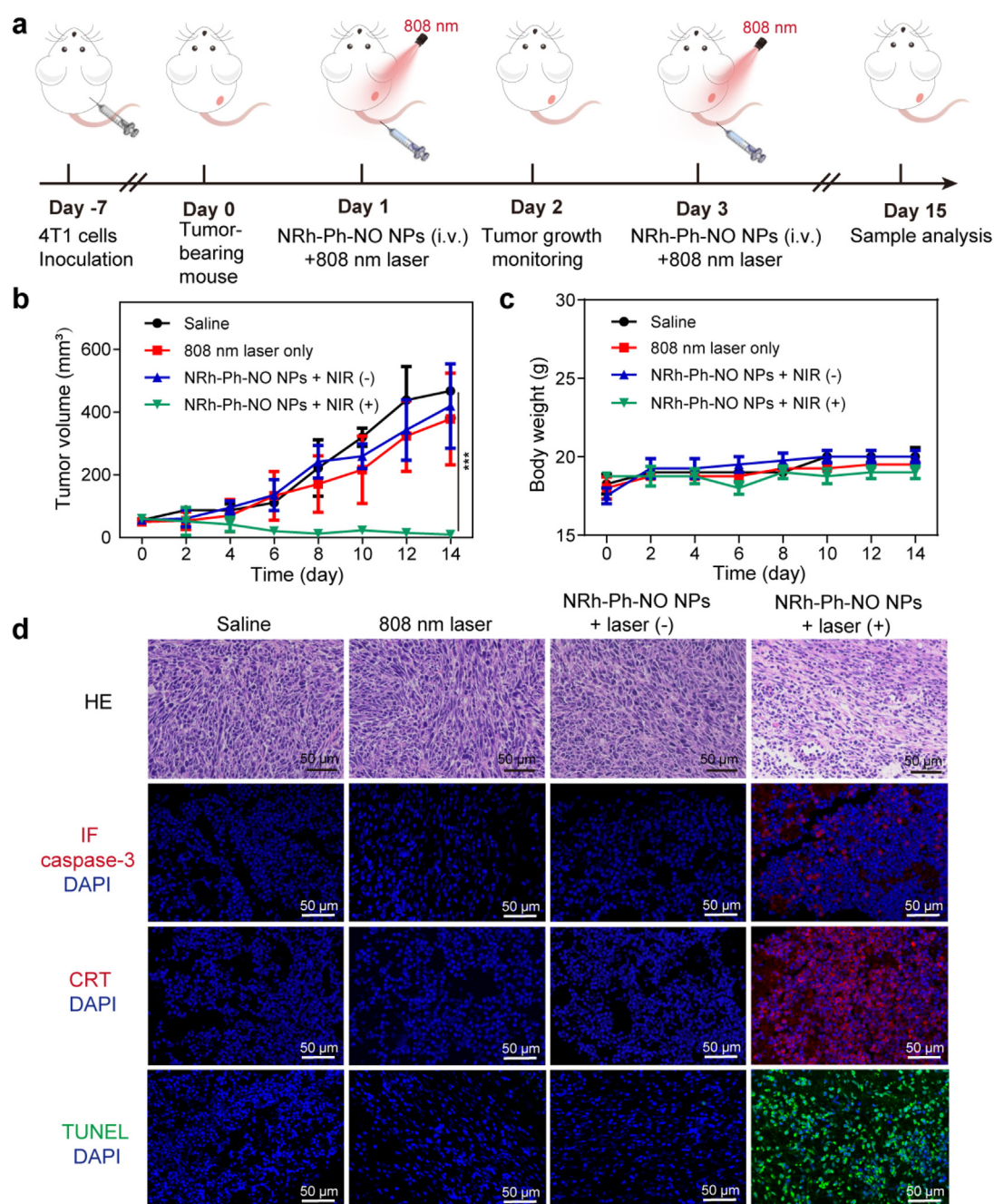


Figure 8 *In vivo* anti-tumor effect of gas therapy with NRh-Ph-NO NPs. (a) Therapeutic schedule of anti-tumor therapy in different groups. The changes of (b) tumor growth and (c) bodyweight during therapy. (d) H&E staining, caspase-3 immunofluorescence (IF) assays (red pseudo-color), CRT expression (red pseudo-color) and TUNEL staining (green pseudo-color) of sections from tumors after different treatments. Scale bar: 50 μm. Data are presented as mean ± SD, $n = 5$.

4. Conclusions

We have successfully developed a series of rhodamine-containing NO donors NRh-R-NO ($R = \text{Me, Et, Bn, } i\text{Pr, and Ph}$) and investigated their photophysical properties. Attachment of the electron-withdrawing *N*-nitroso to rhodamine-inspired NIR dyes resulted in blue-shifted absorption from 720 nm to around 600 nm and quenched emission of 740 nm compared to the precursors. Photo-controlled release studies and theoretical studies revealed that NRh-Ph-NO could effectively release NO and produce a

significant FULC signal at 740 nm under 808 nm light irradiation, attributed to lower N–N bond dissociation energy. Interestingly, the one-for-all gas generator NRh-Ph-NO was activated by 808 nm light to produce superoxide anion $\text{O}_2^{\cdot-}$ and induced highly toxic peroxynitrite anion ONOO^- for RNS-potentiated gas therapy. After the nano-modification, the nanogenerator (NRh-Ph-NO NPs) could be precisely taken up into mitochondria and displayed superior biocompatibility. Significantly, when triggered by an 808 nm laser, NRh-Ph-NO NPs could activate the caspase-3 pathway of apoptosis and trigger tumor immunogenic cell death,

effectively killing cancer cells. Based on FUCL imaging real-time guide, NRh-Ph-NO NPs exhibited extraordinary RNS-potentiated efficacy against tumor eradication *in vivo*. The innovative strategy brings new perspectives to the design of versatile platforms for RNS-mediated therapy of cancer.

Acknowledgments

This work was financially supported by the National Natural Science Foundation of China (82272148, China), the “Double First-Class” University Project (CPUQJNC22-03, China), the Jiangsu Funding Program for Excellent Postdoctoral Talent (2022ZB301, China), the National University of Singapore (NUHSRO/2020/133/Startup/08, NUHSRO/2023/008/NUSMed/TCE/LOA, NUHSRO/2021/034/TRP/09/Nanomedicine), National Medical Research Council (MOH-OFIRG23jan-0005, CG21APR1005), Singapore Ministry of Education (MOE-000387-00), and National Research Foundation (NRF-000352-00).

Author contributions

Hui Yu, Aliya Tiemuer, Hai-Yan Wang, Yi Liu and Xiaoyuan Chen conceived and designed the project. Hui Yu and Aliya Tiemuer performed all experiments and wrote the draft manuscript. Xufeng Yao and Mingyuan Zuo assisted in the *in vivo* experiments. Hui Yu, Hai-Yan Wang, Yi Liu and Xiaoyuan Chen revised the manuscript. All co-authors have given approval to the final version of the manuscript.

Conflicts of interest

The authors declared no conflicts of interest.

Appendix A. Supporting information

Supporting data to this article can be found online at <https://doi.org/10.1016/j.apsb.2023.08.019>.

References

- Li SH, Liu R, Jiang XX, Qiu Y, Song XR, Huang GM, et al. Near-infrared light-triggered sulfur dioxide gas therapy of cancer. *ACS Nano* 2019;**13**:2103–13.
- Bao XY, Zheng SQ, Zhang L, Shen AZ, Zhang GY, Liu SY, et al. Nitric oxide-releasing aza-BODIPY: a new near-infrared *J*-aggregate with multiple antibacterial modalities. *Angew Chem Int Ed Engl* 2022;**61**:e202207250.
- Jiang W, Dong W, Li M, Guo ZX, Wang Q, Liu Y, et al. Nitric oxide induces immunogenic cell death and potentiates cancer immunotherapy. *ACS Nano* 2022;**16**:3881–94.
- Meng J, Jin ZK, Zhao PH, Zhao B, Fan MJ, He QJ. A multistage assembly/disassembly strategy for tumor-targeted CO delivery. *Sci Adv* 2020;**6**:eaba1362.
- Chen LC, Zhou SF, Su LC, Song JB. Gas-mediated cancer bioimaging and therapy. *ACS Nano* 2019;**13**:10887–917.
- Jin ZK, Duo YH, Yang L, Qiu M, Jiang MN, Liu Q, et al. A novel NIR-responsive CO gas-releasing and hyperthermia-generating nanomedicine provides a curative approach for cancer therapy. *Nano Today* 2021;**38**:101197.
- Sun Y, Chen S, Chen XY, Xu YL, Zhang SY, Ouyang QY, et al. A highly selective and recyclable NO-responsive nanochannel based on a spiroring opening-closing reaction strategy. *Nat Commun* 2019;**10**:1323.
- Zhang X, Du JF, Guo Z, Yu J, Gao Q, Yin WY, et al. Efficient near infrared light triggered nitric oxide release nanocomposites for sensitizing mild photothermal therapy. *Adv Sci* 2019;**6**:1801122.
- Chen XH, Jia F, Li YZ, Deng YY, Huang Y, Liu WF, et al. Nitric oxide-induced stromal depletion for improved nanoparticle penetration in pancreatic cancer treatment. *Biomaterials* 2020;**246**:119999.
- Zhang X, Tian G, Yin WY, Wang LM, Zheng XP, Yan L, et al. Controllable generation of nitric oxide by near-infrared-sensitized upconversion nanoparticles for tumor therapy. *Adv Funct Mater* 2015;**25**:3049–56.
- Jie A, Hu YG, Cheng L, Hou XL, Cheng K, Zhang B, et al. A pH/ultrasound dual-response biomimetic nanoplatform for nitric oxide gas-sonodynamic combined therapy and repeated ultrasound for relieving hypoxia. *Biomaterials* 2020;**230**:119636.
- Yuan Z, Lin CC, He Y, Tao BL, Chen MW, Zhang JX, et al. Near-infrared light-triggered nitric-oxide-enhanced photodynamic therapy and low-temperature photothermal therapy for biofilm elimination. *ACS Nano* 2020;**14**:3546–62.
- Wan MM, Chen H, Da Wang Z, Liu ZY, Yu YQ, Li L, et al. Nitric oxide-driven nanomotor for deep tissue penetration and multidrug resistance reversal in cancer therapy. *Adv Sci* 2021;**8**:2002525.
- Wang PZ, Yu L, Gong JK, Xiong JH, Zi SY, Xie H, et al. An activity-based fluorescent probe for imaging fluctuations of peroxynitrite (ONOO⁻) in the Alzheimer's disease brain. *Angew Chem Int Ed* 2022;**61**:e202206894.
- Wu LL, Liu JH, Tian X, Groleau RR, Bull SD, Li P, et al. Fluorescent probe for the imaging of superoxide and peroxynitrite during drug-induced liver injury. *Chem Sci* 2021;**12**:3921–8.
- Hou JT, Yu KK, Sunwoo K, Kim WY, Koo S, Wang JY, et al. Fluorescent imaging of reactive oxygen and nitrogen species associated with pathophysiological processes. *Chem* 2020;**6**:832–66.
- Zhang W, Liu JH, Li P, Wang X, Bi SM, Zhang J, et al. *In situ* and real-time imaging of superoxide anion and peroxynitrite elucidating arginase 1 nitration aggravating hepatic ischemia-reperfusion injury. *Biomaterials* 2019;**225**:119499.
- Ieda N, Nakagawa H, Peng T, Yang D, Suzuki T, Miyata N. Photo-controllable peroxynitrite generator based on *N*-methyl-*N*-nitrosoaminophenol for cellular application. *J Am Chem Soc* 2012;**134**:2563–8.
- Deng YY, Wang YP, Jia F, Liu WF, Zhou DF, Jin Q, et al. Tailoring supramolecular prodrug nanoassemblies for reactive nitrogen species-potentiated chemotherapy of liver cancer. *ACS Nano* 2021;**15**:8663–75.
- Feng Y, Zhang HX, Xie XX, Chen Y, Yang G, Wei XD, et al. Cascade-activatable NO release based on GSH-detonated “nanobomb” for multi-pathways cancer therapy. *Mater Today Bio* 2022;**14**:100288.
- Wang PG, Xian M, Tang XP, Wu XJ, Wen Z, Cai TW, et al. Nitric oxide donors: chemical activities and biological applications. *Chem Rev* 2002;**102**:1091–134.
- Fan WP, Yung BC, Chen XY. Stimuli-responsive NO release for on-demand gas-sensitized synergistic cancer therapy. *Angew Chem Int Ed* 2018;**57**:8383–94.
- He HH, He TT, Zhang ZQ, Xu X, Yang HB, Qian XH, et al. Ring-restricted *N*-nitrosated rhodamine as a green-light triggered, orange-emission calibrated and fast-releasing nitric oxide donor. *Chin Chem Lett* 2018;**29**:1497–9.
- Duan YT, Wang Y, Li XH, Zhang GZ, Zhang GY, Hu JM. Light-triggered nitric oxide (NO) release from photoresponsive polymer-somes for corneal wound healing. *Chem Sci* 2020;**11**:186–94.
- Sun J, Cai XT, Wang CJ, Du K, Chen WJ, Feng FD, et al. Cascade reactions by nitric oxide and hydrogen radical for anti-hypoxia photodynamic therapy using an activatable photosensitizer. *J Am Chem Soc* 2021;**143**:868–78.
- Xu Y, Li H, Xu SF, Liu X, Lin JJ, Chen HY, et al. Light-triggered fluorescence self-reporting nitric oxide release from coumarin analogues for accelerating wound healing and synergistic antimicrobial applications. *J Med Chem* 2022;**65**:424–35.
- Jiang LD, Chen DY, Jin ZK, Xia C, Xu QQ, Fan MJ, et al. Light-triggered nitric oxide release and structure transformation of peptide for enhanced intratumoral retention and sensitized photodynamic therapy. *Bioact Mater* 2022;**12**:303–13.

28. Zhang K, Xu HX, Jia XQ, Chen Y, Ma M, Sun LP, et al. Ultrasound-triggered nitric oxide release platform based on energy transformation for targeted inhibition of pancreatic tumor. *ACS Nano* 2016;**10**:10816–28.
29. Wang YB, Yang XW, Chen XB, Wang X, Wang Y, Wang HC, et al. Sustained release of nitric oxide and cascade generation of reactive nitrogen/oxygen species via an injectable hydrogel for tumor synergistic therapy. *Adv Funct Mater* 2022;**32**:2206554.
30. Zhou EY, Knox HJ, Reinhardt CJ, Partipilo G, Nilges MJ, Chan J. Near-infrared photoactivatable nitric oxide donors with integrated photoacoustic monitoring. *J Am Chem Soc* 2018;**140**:11686–97.
31. Ye J, Jiang JK, Zhou ZR, Weng ZZ, Xu YY, Liu LB, et al. Near-infrared light and upconversion nanoparticle defined nitric oxide-based osteoporosis targeting therapy. *ACS Nano* 2021;**15**:13692–702.
32. Zheng Y, Ye ZW, Liu ZJ, Yang W, Zhang XF, Yang YJ, et al. Nitroso-caged rhodamine: a superior green light-activatable fluorophore for single-molecule localization super-resolution imaging. *Anal Chem* 2021;**93**:7833–42.
33. Zhao XZ, Long S, Li ML, Cao JF, Li YC, Guo LY, et al. Oxygen-dependent regulation of excited-state deactivation process of rational photosensitizer for smart phototherapy. *J Am Chem Soc* 2020;**142**:1510–7.
34. Feng T, Wan JY, Li P, Ran HT, Chen HL, Wang ZG, et al. A novel NIR-controlled NO release of sodium nitroprusside-doped Prussian blue nanoparticle for synergistic tumor treatment. *Biomaterials* 2019;**214**:119213.
35. Liu Y, Su QQ, Zou XM, Chen M, Feng W, Shi YB, et al. Near-infrared *in vivo* bioimaging using a molecular upconversion probe. *Chem Commun* 2016;**52**:7466–9.
36. Yu H, Sun W, Tiemuer A, Zhang YY, Wang HY, Liu Y. Mitochondria targeted near-infrared chemodosimeter for upconversion luminescence bioimaging of hypoxia. *Chem Commun* 2021;**57**:5207.
37. Yu H, Tiemuer A, Zhu YY, Sun Y, Zhang YY, Liu L, et al. Albumin-based near-infrared phototheranostics for frequency upconversion luminescence/photoacoustic dual-modal imaging-guided photothermal therapy. *Biomater Sci* 2023;**11**:4574–82.
38. Zhu W, Yu H, Qian X, Lu K, Zhao C, Zhang YY, et al. Near-infrared frequency upconversion probe for revealing the relationship between glutathione S-transferase and drug-resistance. *Anal Chim Acta* 2021;**1181**:338920.
39. Zhang Y, Wang J, Sun W, Yu H, An S, Wang HY, et al. Mitochondria targeted upconversion molecular platform for photodynamic therapy of cancer cells. *Dyes Pigm* 2022;**208**:110753.
40. Yu H, Wang Q, Zhang XM, Tiemuer A, Wang J, Zhang Y, et al. Hot-band absorption assisted single-photon frequency upconversion luminescent nanophotosensitizer for 808 nm light triggered photodynamic immunotherapy of cancer. *Biomater Sci* 2023;**11**:2167–76.
41. Liu Y, Su QQ, Chen M, Dong Y, Shi YB, Feng W, et al. Near-infrared upconversion chemodosimeter for *in vivo* detection of Cu²⁺ in wilson disease. *Adv Mater* 2016;**28**:6625–30.
42. Tiemuer A, Yu H, Zhao C, Sun W, Zhang YY, Jiang Y, et al. Nitroso-caged upconversion luminescent prodrug: near infrared light-activatable NO nano-donor for gas therapy. *Chem Eng J* 2022;**430**:132858.
43. Yang HR, Han CM, Zhu XJ, Liu Y, Zhang KY, Liu SJ, et al. Upconversion luminescent chemodosimeter based on NIR organic dye for monitoring methylmercury *in vivo*. *Adv Funct Mater* 2016;**26**:1945–53.
44. Wang H, Liu Y, Wang ZH, Yang M, Gu YQ. 808 nm-light-excited upconversion nanoprobe based on LRET for the ratiometric detection of nitric oxide in living cancer cells. *Nanoscale* 2018;**10**:10641–9.
45. Akaie T, Yoshida M, Miyamoto Y, Sato K, Kohno M, Sasamoto K, et al. Antagonistic action of imidazolineoxyl *N*-oxides against endothelium-derived relaxing factor/ \bullet NO through a radical reaction. *Biochemistry* 1993;**32**:827–32.
46. Wu D, Ryu JC, Chung YW, Lee D, Ryu JH, Yoon JH, et al. A far-red-emitting fluorescence probe for sensitive and selective detection of peroxynitrite in live cells and tissues. *Anal Chem* 2017;**89**:10924–31.
47. Krishnan R, Binkley JS, Seeger R, Pople JA. Self-consistent molecular orbital methods. XX. A basis set for correlated wave functions. *J Chem Phys* 1980;**72**:650–4.
48. Burke K. Perspective on density functional theory. *J Chem Phys* 2012;**136**:150901.
49. Li ML, Xiong T, Du JJ, Tian RS, Xiao M, Guo LY, et al. Superoxide radical photogenerator with amplification effect: surmounting the achilles' heels of photodynamic oncology. *J Am Chem Soc* 2019;**141**:2695–702.
50. Teng KX, Chen WK, Niu LY, Fang WH, Cui GL, Yang QZ. BODIPY-based photodynamic agents for exclusively generating superoxide radical over singlet oxygen. *Angew Chem Int Ed Engl* 2021;**60**:19912–20.
51. Yu FZ, Shao YL, Chai X, Zhao YL, Li LL. Spatially selective monitoring of subcellular enzyme dynamics in response to mitochondria-targeted photodynamic therapy. *Angew Chem Int Ed Engl* 2022;**61**:e202203238.
52. Gao G, Jiang YW, Zhan WJ, Liu XY, Tang RQ, Sun XB, et al. Trident molecule with nanobrush–nanoparticle–nanofiber transition property spatially suppresses tumor metastasis. *J Am Chem Soc* 2022;**144**:11897–910.